Accelerated Discovery of Large Electrostrains in BaTiO$_3$-Based Piezoelectrics Using Active Learning

Ruihao Yuan, Zhen Liu, Prasanna V. Balachandran, Deqing Xue, Yumei Zhou, Xiangdong Ding, Jun Sun, Dezhen Xue,* and Turab Lookman*

A key challenge in guiding experiments toward materials with desired properties is to effectively navigate the vast search space comprising the chemistry and structure of allowed compounds. Here, it is shown how the use of machine learning coupled to optimization methods can accelerate the discovery of new Pb-free BaTiO$_3$ (BTO-) based piezoelectrics with large electrostrains. By experimentally comparing several design strategies, it is shown that the approach balancing the trade-off between exploration (using uncertainties) and exploitation (using only model predictions) gives the optimal criterion leading to the synthesis of the piezoelectric (Ba$_{0.84}$Ca$_{0.16}$)(Ti$_{0.90}$Zr$_{0.07}$Sn$_{0.03}$)O$_3$ with the largest electrostrain of 0.23% in the BTO family. Using Landau theory and insights from density functional theory, it is uncovered that the observed large electrostrain is due to the presence of Sn, which allows for the ease of switching of tetragonal domains under an electric field.

Finding new materials with targeted properties with as few experiments as possible is a key goal of accelerated materials discovery.[1–4] The enormous complexity due to the interplay of structural, chemical, and microstructural degrees of freedom in materials makes the rational design of new materials with targeted properties rather difficult.[5] First principles high throughput calculations at 0 K have largely been used to generate large amounts of data to screen for promising candidates for further study.[6–9] Machine learning and optimal experimental design, used in industry for solving complex problems, in fields such as pattern recognition, bioinformatics, and operations research,[8–10] are being adapted for the design of new materials.[2–4,11,12] The machine learning algorithms effectively learn from past data and build an inference model relating the targeted property to material descriptors.[3,12–14] The targeted properties of unexplored materials are then estimated, leading to the rational choice of the next experiment or

calculation. However, the number of well-characterized samples available as sources of data to learn from is typically small; as a result, uncertainties associated with the predictions from model fits, or even those from measurements, become large and important. The choice of the next experiment or calculation solely based on the inference model predictions is prone to be suboptimal.[9] Thus, optimization schemes are needed for decision making to guide experiments using uncertainties to explore the vast material space in an active learning loop to successively improve predictions to minimize the number of measurements needed.[14–16]

Few studies have demonstrated an active learning framework that iteratively combines machine learning, optimization, and experiments.[2,4,11] Recently, we studied a number of active learning strategies for their appropriateness on materials data sets[3] and have shown how such algorithms can be used to find new materials, such as alloys.[4] However, lacking is any work comparing how different optimization or design methods perform experimentally when guiding the next experiments toward the targeted objectives. Here we address this challenge by demonstrating the discovery of superior Pb-free BaTiO$_3$ (BTO) based piezoelectrics with large electrostrains. In particular, we show how our optimal experimental design approach leads to the piezoelectric (Ba$_{0.84}$Ca$_{0.16}$)(Ti$_{0.90}$Zr$_{0.07}$Sn$_{0.03}$)O$_3$ with the largest electrostrain of 0.23% (unipolar strain 0.19%) under a field of 20 kV cm^{-1} in the BTO family. Using Landau theory in particular, and insights from density functional theory (DFT), we show that the physics underlying this composition is controlled by Sn^{4+} that facilitates the switching of tetragonal domains under the action of an external electric field. We demonstrate experimentally that balancing the trade-off between exploration (using uncertainties) and exploitation (using only inference model predictions) gives the optimal criterion for the design of the next experiment, especially when the initial size of data is limited.

High-performance actuator materials, such as electroceramics, convert electrical energy to mechanical strain through either piezoelectricity or electrostriction.[17–19] They are desired for a wide range of applications such as micromotors and prosthetic devices.[20–24] In particular, the Pb-based family of perovskites has been the ceramics of choice, but toxicity associated with Pb has led to recent efforts to find alternatives.[25–29]

R. Yuan, D. Xue, Dr. Y. Zhou, Prof. X. Ding, Prof. J. Sun, Dr. D. Xue
State Key Laboratory for Mechanical Behavior of Materials
Xi'an Jiaotong University
Xi'an 710049, China
E-mail: xuedezhen@mail.xjtu.edu.cn
Z. Liu, Dr. P. V. Balachandran, Prof. T. Lookman
Theoretical Division
Los Alamos National Laboratory
Los Alamos, NM 87545, USA
E-mail: txl@lanl.gov

The BTO-based family, such as the well-studied compound $(Ba_{0.85}Ca_{0.15})(Ti_{0.90}Zr_{0.10})O_3$ (BCT-0.5BZT), shows considerable promise as it has both large piezoelectricity ($d_{33} \approx 620$ pC N^{-1}) and electrostrictive strain coefficient ($Q_{33} \approx 0.045$ m^4 C^{-2}), and these compounds lend themselves to ease of operation at low voltages.[30–32] Thus, as our design criterion we focus on searching for BTO-based electroceramics with large electrostrain. Our strategy is to enhance the electrostrain by chemical substitution (i.e., dopants) with Ca^{2+} and Sr^{2+} cations replacing Ba^{2+}, and Zr^{4+}, and Sn^{4+} substituting for Ti^{4+} in BTO. The family of solid solutions is thus given by $(Ba_{1.0-x-y}Ca_xSr_y)$ $(Ti_{1.0-u-v}Zr_uSn_v)O_3$, where the mole fractions x, y, u, and v are constrained by $1-x-y>0.6$, $x<0.4$, $y<0.3$, $1-u-v>0.6$, $u<0.3$, and $v<0.3$ to avoid the possible presence of relaxor phases. As the composition of each ion can be controlled to 0.01 in the synthesis process, there are potentially $\approx605\,000$ possible compositions of which only 61 have been synthesized ($\approx0.01\%$). This is a vast search space that cannot be explored by mere trial and error and intuition. Required is a systematic material design strategy to guide or recommend iteratively the optimal compounds for synthesis.

Figure 1 illustrates our material design active learning loop and shows the four search methodologies to guide experiments that we compare in this work. The data of known samples from which the initial learning occurs (*training* data) consist of the measured property (bipolar electrostrain at 20 kV cm^{-1}) and material descriptors or features. The features, which should be easily available for all unexplored materials, are expected to be physically meaningful and should have a bearing on the property. We choose elemental and structural properties such as electronegativity, ionic radii, ideal bond distance, and tolerance factor as these impact polarization and strain, and the contributions from the A and B sites of the perovskite unit cell are determined by mole fraction of the elements. We also included products and ratios of the A and B site features to give us a total of 71 features (Section S1, Supporting Information). Eliminating pairs of features that are strongly correlated (in excess of a Pearson correlation coefficient of 0.95; see Section S2, Supporting Information) reduces the total number of features to 18. For example, only the tolerance factor is retained as it is correlated with the ideal bond distance. Since not all features are equally important, we invoked the method of gradient boosting in machine learning (see Section S2, Supporting Information) to rank the remaining features. This method trains regression models using data samples that are "difficult" to learn in other models, which results in an ensemble of models that are good at learning different "parts" of the training data.[13] Those features which ranked highly included the direction (increase, decrease, or no change) of the dependence of the cubic to tetragonal ferroelectric transition temperature, NCT, and tetragonal to orthorhombic ferroelectric transition temperature, NTO, on the doping elements. For example, addition of Zr to $BaTiO_3$ decreases the C–T transition temperature (NCT = −1) and increases the T–O transition temperature (NTO = +1). We
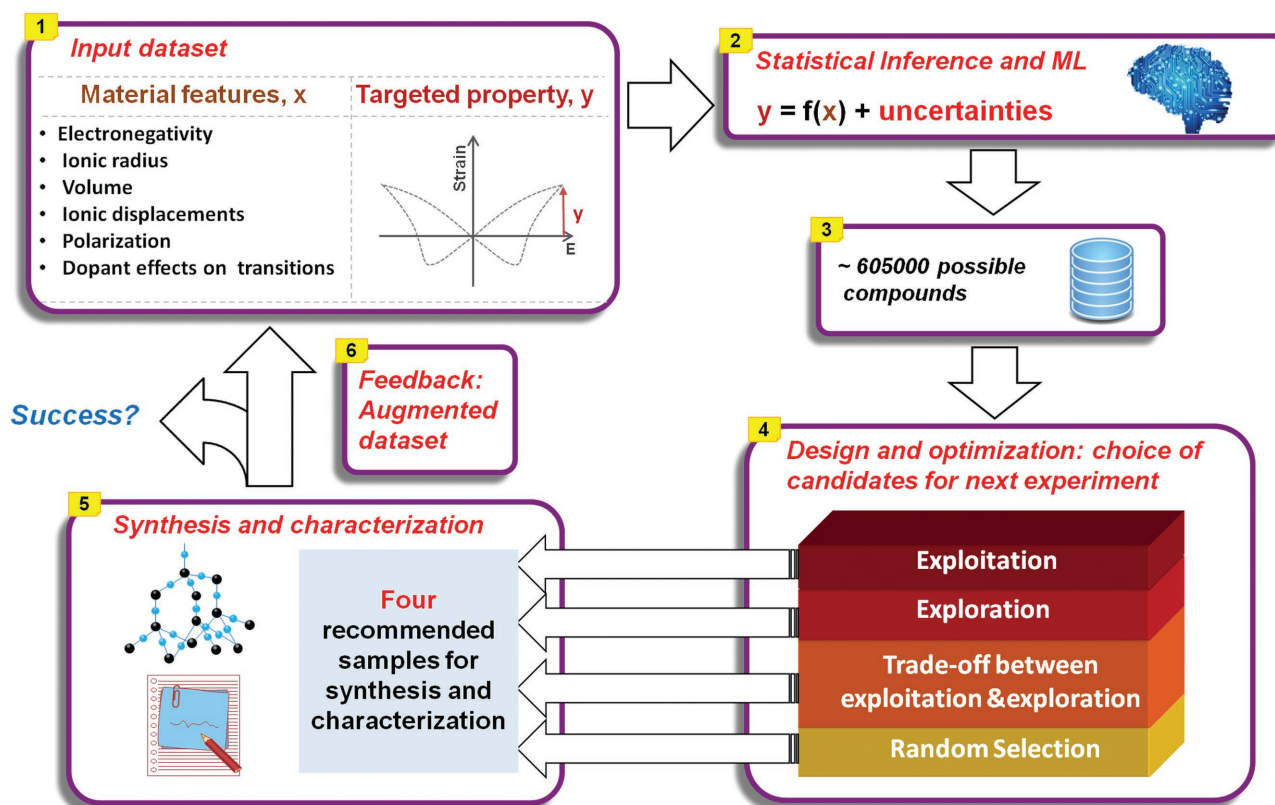

Figure 1. Our active learning loop for accelerated discovery based on machine learning and optimal experimental design to iteratively guide experiments in the search for high-performance piezoelectrics with large electrostrains. Compounds are synthesized following predictions from four strategies (exploitation, exploration, trade-off between the former two, and random selection), the performance of which are compared.

next trained an empirical, statistical inference model, $y = f(x)$, on the data to predict the electrostrains, y, from a knowledge of the preselected features, x, where f is the estimated or learned relationship. This serves as a surrogate model in the absence of a physics based model for this mapping. We compared the performance of several linear, nonlinear, and kernel based inference models on the dataset to identify those with the least cross-validation error on unseen data using standard machine learning approaches (see Section S3, Supporting Information). The support vector regression model with a radial basis function kernel was the best performer in estimating f and we used it to make predictions of the electrostrain on the $\approx$605 000 unexplored compositions.

If machine learning is all we were doing, we would utilize the best predictions from the database of unexplored compositions for synthesis. However, this is not necessarily the optimal strategy. A key element in our work compared to the current state-of-the-art in materials design is adaptive experimental design through which we determine iteratively the optimal compounds for synthesis, and these are not necessarily the best predicted from regression via machine learning. It is the adaptive aspect that gives rise to active learning. A central idea we employ is the use of uncertainties to explore the search space for the next best candidate.[14,33] We have used the approach that balances the trade-off between the best from inference or regression ("exploitation") and by considering the maximum uncertainty in the predictions ("exploration").[33] However, the merits of a purely exploitative or exploratory strategy, or the choice of the next compound for synthesis based on a trade-off between the two, has not been studied previously, certainly not experimentally. Such optimization or active or reinforcement learning methods have been tested on special functions or on the output of computer codes and their performance compared.[33] Here we will test these experimentally to identify, at least for the electrostrain problem, the best performing adaptive design method. To the three strategies mentioned, we also add the selection of a composition for synthesis based on a purely random choice from all the allowed possibilities. Thus, we will compare experimentally the merits of four strategies: exploitation, exploration, trade-off between exploitation and exploration, and random choice (see Section S4, Supporting Information). The trial and intuition approach that seeks to extrapolate trends in data could be seen as similar to exploitation, where the best prediction from inference is used.

We evaluated the inference model uncertainties using the statistical method of "bootstrap" sampling, in which sample compositions from the training dataset are randomly generated allowing for replacements. Each new data set then leads to a model with its own predictions, and by treating the uncertainties from 1000 bootstrap samples as the realization of a normally distributed variable, we can estimate the mean (μ) and standard deviations (σ) of the predictions. For simplicity, in this work we do not incorporate measurement uncertainties. The idea then is to maximize the "expected improvement," $E(I)$, the ranking criterion, which ensures that the search will combine exploration and exploitation, i.e., explores the total search space where the uncertainties are the largest and exploits where the uncertainties are small but the mean is large, guiding the search to find the global optimum. The improvement, $I = Y - \mu*$,

where Y is a random variable for electrostrain chosen from a distribution where the uncertainties are assumed to be normally distributed with mean, μ, with standard deviation, σ, and where $\mu*$ is the mean of the "best-so-far" value of the electrostrain, assuming it is a maximum. Thus, $E(I)$ gives the probability of making improvements to the current best estimate of the electrostrain by sampling from compounds in the search space using the uncertainties in electrostrain estimates. The sample with the largest $E(I)$ is then chosen for the next experiment. With $E(I) = \int I\phi(z)dz = \sigma[\phi(z) + z\Phi(z)]$, where $z = (\mu - \mu*)/\sigma$ and $\phi(z)$ and $\Phi(z)$ are the standard normal density and cumulative distribution functions, respectively, in the limit $\sigma \to 0$ (no uncertainty), $E(I) = \mu - \mu*$, so that we choose compositions with $\mu >$ best-so-far ($\mu*$) to maximize $E(I)$ – exploitation. Similarly, for $\sigma \to \infty$, $E(I) \approx \sigma$, and the choice will be limited to those samples with the largest uncertainty – exploration. For σ between 0 and ∞, there will be a trade-off between the extremes of exploitation and exploration. Clearly, the expected improvement is not only related to the average predicted value (μ) but also to the uncertainty (σ) and maximizing expected improvement provides an optimal means to trade-off between the two extremes.[33]

Figure 2a shows the results from synthesis and characterization of the compounds predicted by each of our chosen design methods. We performed the iterative feedback loop a total of five times, thus five compounds were predicted and synthesized by each of the four methods (20 compounds in total and these are listed in **Table 1**). After each iteration, the electrostrains of the new compounds were measured and the results augmented the training data leading to a new round of regression and design. We note that we find a composition with large electrostrain at 20 kV cm^{-1} after just one iteration, which is better than the best in the training data. On the third iteration the compound $(Ba_{0.84}Ca_{0.16})(Ti_{0.90}Zr_{0.07}Sn_{0.03})O_3$ with the largest electrostrain was obtained. The strategy based on a trade-off between exploitation and exploration (referred to as efficient global optimization[33]) performs in a superior manner to the others. It produced the best performer in every iteration. The predictions from our design shown in Figure 2b deviate slightly from the measured values, however, the trend and largest strain obtained are roughly similar. The quality of our model predictions are shown in Figure 2c, which compares the electrostrains of all predicted and measured compounds from the training data and those obtained in successive iterations. There is enough scatter around the diagonal line to suggest that the model is certainly not overfitting and the agreement is reasonable. From Figure 2a, the strategy of random selection of a compound for synthesis is the worst performer and the pure exploitation strategy is superior to the one based on pure exploration. The exploitation strategy searches in the neighborhood of local minima in the feature landscape, and this appears for this problem to be preferred to exploration, which searches in regions where the uncertainties are largest, for example, where there is little data. Of the 20 compounds synthesized, 9 had larger electrostrains than the best in the training set (Table 1), giving a Fisher p value < 0.001, that is, the probability that the best performing compounds came from a random distribution similar to the training compound, is very low.
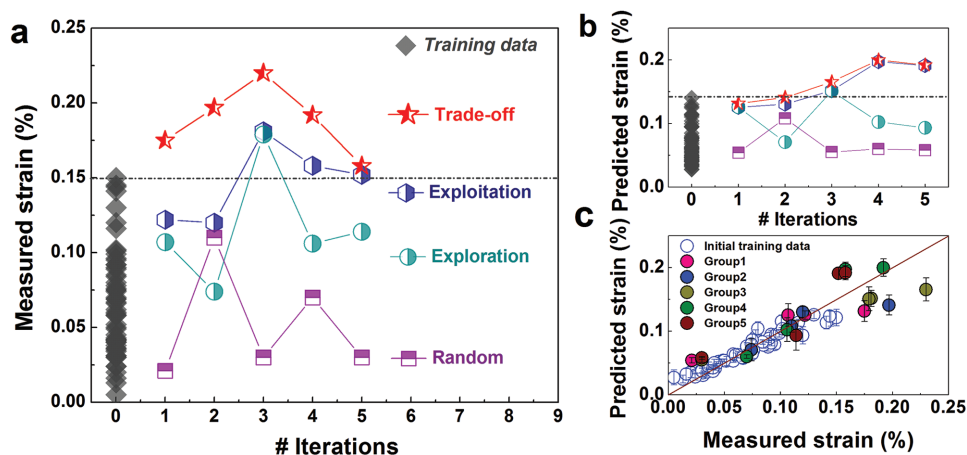
Figure 2. The results of the inference and design. a) Experimental comparison of the four design methodologies showing that the trade-off between exploration and exploitation performs better at each iteration than the other strategies in finding the compound with the largest electrostrains. b) The predictions from our method. c) The predicted and measured electrostrains of the new synthesized compounds are in reasonable agreement and provide confidence in the quality of the inference model.

Figure 3a shows the measured butterfly-like strain versus electric field curve of the best compound $(Ba_{0.84}Ca_{0.16})(Ti_{0.90}Zr_{0.07}Sn_{0.03})O_3$ obtained in the third iteration, where it is compared to the best in the training data $(Ba_{0.84}Ca_{0.16})(Ti_{0.90}Zr_{0.10})O_3$, as well as the prototypical compound, $(Ba_{0.85}Ca_{0.15})(Ti_{0.90}Zr_{0.10})O_3$ (BCT-0.5BZT). The bipolar electrostrain is 0.23%, enhanced by 53.3% compared to the best in the training data at $E = 20$ kV cm^{-1}, although the ferroelectric

polarization hysteresis loops of the two almost overlap (Figure S6, Supporting Information). The electrostrains were measured by an MTI2000 photonic sensor and the electrostrictive coefficient, Q_{33}, relating the strain ε_{33} with polarization P_3 by $\varepsilon_{33} = Q_{33}P_3^2$, is measured to be 0.106 m^4 C^{-2} at 20 kV cm^{-1}. Our new composition $(Ba_{0.84}Ca_{0.16})(Ti_{0.90}Zr_{0.07}Sn_{0.03})O_3$ (hereafter referred to as 3 at% Sn) substitutes 3 at% Zr with Sn compared to the best in the training data $(Ba_{0.84}Ca_{0.16})(Ti_{0.90}Zr_{0.10})O_3$

Table 1. The 20 newly predicted and synthesized compounds with measured maximum bipolar strains at $E = 20$ kV cm^{-1} and electrostrictive coefficient, Q_{33}. The composition in bold discovered in interation #3 is the best performer.

| Iteration no.	Composition	Strain [%]	Q_{33} [m^4 C^{-2}]
1	$(Ba_{0.88}Ca_{0.12})(Ti_{0.92}Zr_{0.03}Sn_{0.05})O_3$	0.122	0.040
1	$(Ba_{0.83}Ca_{0.17})(Ti_{0.92}Zr_{0.08})O_3$	0.107	0.057
1	$(Ba_{0.84}Ca_{0.16})(Ti_{0.91}Zr_{0.08}Sn_{0.01})O_3$	0.175	0.069
1	$(Ba_{0.78}Ca_{0.13}Sr_{0.09})(Ti_{0.83}Sn_{0.17})O_3$	0.021	–
2	$(Ba_{0.87}Ca_{0.13})(Ti_{0.91}Zr_{0.04}Sn_{0.05})O_3$	0.120	0.040
2	$(Ba_{0.86}Ca_{0.14})(Ti_{0.87}Zr_{0.13})O_3$	0.074	0.046
2	$(Ba_{0.85}Ca_{0.15})(Ti_{0.90}Zr_{0.07}Sn_{0.03})O_3$	0.197	0.092
2	$(Ba_{0.92}Ca_{0.08})(Ti_{0.91}Zr_{0.01}Sn_{0.08})O_3$	0.110	0.043
3	$(Ba_{0.85}Ca_{0.15})(Ti_{0.91}Zr_{0.05}Sn_{0.04})O_3$	0.181	0.070
3	$(Ba_{0.84}Ca_{0.16})(Ti_{0.89}Zr_{0.07}Sn_{0.04})O_3$	0.179	0.083
3	$\mathbf{(Ba_{0.84}Ca_{0.16})(Ti_{0.90}Zr_{0.07}Sn_{0.03})O_3}$	**0.230**	**0.106**
3	$(Ba_{0.76}Ca_{0.08}Sr_{0.16})(Ti_{0.85}Zr_{0.06}Sn_{0.09})O_3$	0.030	–
4	$(Ba_{0.84}Ca_{0.16})(Ti_{0.90}Zr_{0.06}Sn_{0.04})O_3$	0.158	0.055
4	$(Ba_{0.85}Ca_{0.15})(Ti_{0.87}Zr_{0.06}Sn_{0.07})O_3$	0.106	0.047
4	$(Ba_{0.83}Ca_{0.17})(Ti_{0.90}Zr_{0.07}Sn_{0.03})O_3$	0.192	0.077
4	$(Ba_{0.74}Ca_{0.11}Sr_{0.15})(Ti_{0.92}Zr_{0.03}Sn_{0.05})O_3$	0.070	0.061
5	$(Ba_{0.84}Ca_{0.15}Sr_{0.01})(Ti_{0.90}Zr_{0.07}Sn_{0.03})O_3$	0.152	0.031
5	$(Ba_{0.83}Ca_{0.17})(Ti_{0.90}Zr_{0.03}Sn_{0.07})O_3$	0.114	0.054
5	$(Ba_{0.84}Ca_{0.16})(Ti_{0.90}Zr_{0.08}Sn_{0.02})O_3$	0.158	0.072
5	$(Ba_{0.70}Ca_{0.18}Sr_{0.12})(Ti_{0.67}Zr_{0.22}Sn_{0.11})O_3$	0.030	–
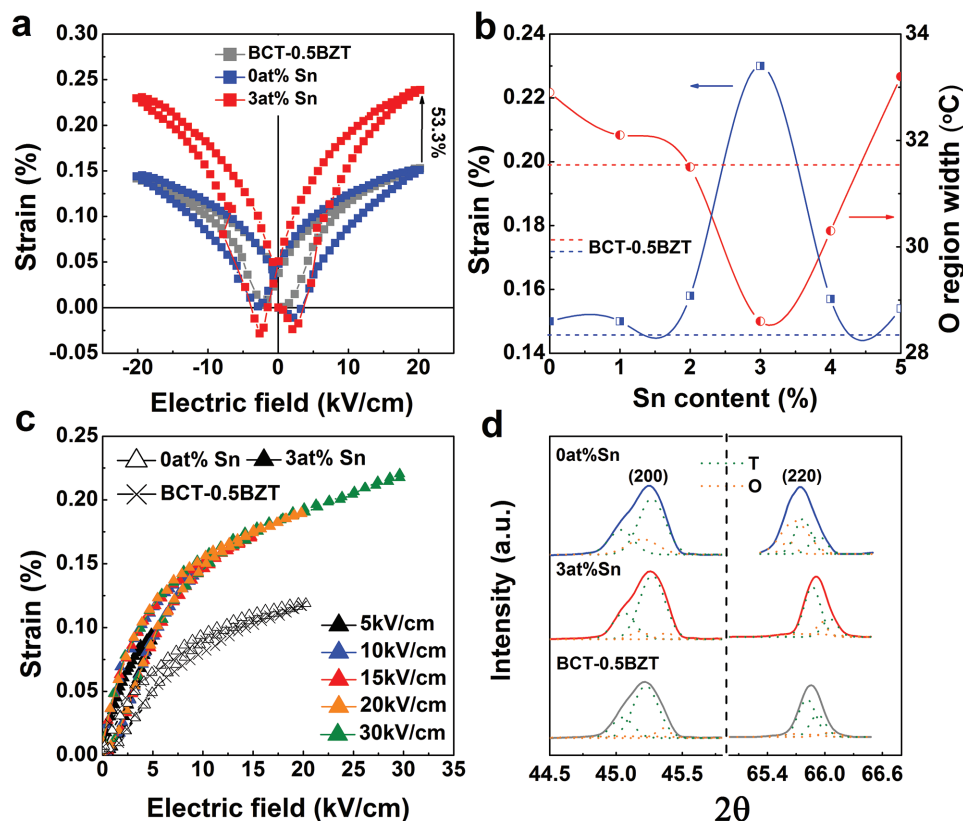
Figure 3. Validation of the predictions of our inference and design. a) The measured dependence of the electrostrain on the external electric field for the optimal compound. At 20 kV cm^{-1}, the bipolar strain (0.23%) for the 3 at% Sn compound is larger than that for the 0 at% Sn compound (0.15%), the best in our training data, or that of BCT-0.5BZT (0.145%). b) Strain and orthorhombic region width (in temperature) from the data in Figure S8 (Supporting Information) as a function of Sn content, showing that the 3 at% Sn compound is optimal, dashed lines correspond to those for BCT-0.5BZT. c) The unipolar electrostrain curves for the third cycle for 3 at% Sn, 0 at% Sn, and BCT-0.5BZT compounds under different electric fields. d) Characteristic diffraction peaks for the three compounds BCT-0.5BZT, 0 at% Sn, and 3 at% Sn at room temperature indicate coexisting tetragonal and orthorhombic phases.

(0 at% Sn), but both have the same total A site and B site dopant concentrations (16 at% for A site and 10 at% for B site). In order to understand the salient physics leading to our optimal compound, we measured the bipolar electrostrain as a function of Sn concentration from 1 to 5 at%. Figure 3b shows that the electrostrain is a maximum at the 3 at% Sn composition, as predicted by our method. Our design loop thus captures the composition where the targeted electrostrain is optimal. There is potential for further improvement by grain size engineering, texturing or by growing single crystals. We do not consider these aspects in this work. Moreover, the elastic constants as a function of Sn composition did not show any unusual elastic instability at this optimal composition (Figure S5, Supporting Information). However, the width of the orthorhombic region in the phase diagram, as determined from the peaks in the dielectric permittivity and loss tan δ data, is smallest at the 3 at% Sn composition and increases on either side, mirroring the electrostrain behavior (Figure 3b). The shrinking in temperature interval of the O phase region is connected with the flattening of the free energy profile of the T and R phases and favors the smaller polarization anisotropy (see also ref. [34]; we discuss this in Figure 5a). For applications, as in devices such

as multilayer capacitors and electrostrictive actuators, characteristics of unipolarly induced strains are of greater practical importance than those of bipolarly induced strains. We plot in Figure 3c the unipolar strain obtained for the third cycle (the second cycle still has a small remnant strain of 0.016%; see Section S5, Supporting Information) and compare to the bipolar strain shown in Figure 3a. The value of the maximum unipolar electrostrain of the 3 at% Sn compound at 20 kV cm^{-1} is 0.19%, consistent with the larger value of 0.23% from the measured butterfly-like strain curve. In addition, the unipolar strain for the BCT-0.5BZT compound at 20 kV cm^{-1} is 0.115%, slightly lower than the value of 0.12% for 0 at% Sn. The diffraction peak signatures in Figure 3d suggest coexisting tetragonal and orthorhombic phases, and as the T to O phase transition temperatures are below room temperature (see Section S5, Supporting Information), this indicates that the O phase is metastable. This is consistent with our calculated minimum free energy profile in Figure S13 (Supporting Information), which shows that the O phase in the 3 at% Sn is more unstable than the other two compounds. To compare a figure of merit across several piezoelectric classes, we plot in **Figure 4** the maximum unipolar electrostrain versus the large-signal piezoelectric

ADVANCED
SCIENCE NEWS
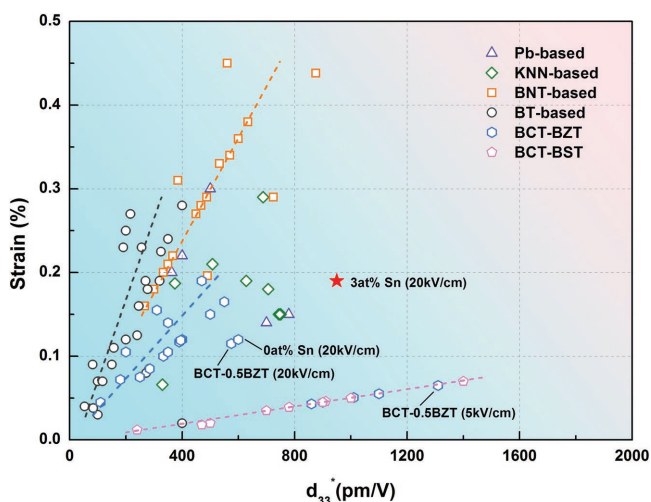www.advancedsciencenews.com

ADVANCED
MATERIALS
www.advmat.de

Figure 4. Unipolar strain as a function of large field $d_{33}* = S_{max}/E_{max}$ for piezoelectric solid solutions including the BT-based, BNT-based, KNN-based, lead-based families, and the Sn-doped compounds in this work.

coefficient ($d_{33}* = S_{max}/E_{max}$) for our Sn-doped compound relative to other lead-free and lead-based ceramics.[35–37] The compound with 3 at% Sn shows superior performance in terms of balancing both large unipolar strain and large $d_{33}*$.

To provide an understanding of the physics controlling the large electrostrain in the 3 at% Sn compound, we performed DFT calculations at Temperature = 0 K (see Computational Section). We used a supercell of 60 atoms (12 Ba, 12 Ti, and 36 O atoms) and substituted one Zr (or Sn) for Ti in the perovskite lattice to mimic the solid solution. The nominal composition of the simulated cell then is Ba(Ti$_{0.92}$X$_{0.08}$)O$_3$, where X = Zr or Sn. Although we do not simulate the exact compositions experimentally prepared, the purpose of the DFT is to glean qualitative insights into a complex problem at the atomic level. Our DFT results for the three perovskite structures cubic (C), tetragonal (T), and orthorhombic (O), for which we compute the energy differences, lattice strains, spontaneous polarization, and electrostrictive coefficients, are summarized in Table S2 (Supporting Information). In general, we find that the total energy for the O structure is lower than T, which in turn is lower than C. More specifically, the energy difference between O and T for the Sn compound is smaller than that for the Zr compound, suggesting that the stability field for the T phase in Sn compound is relatively smaller compared to that in the Zr compound. However, this does not take into account energy barriers from O to T or the thermodynamics of the transformation. The lattice strains in T are also larger compared to O ($\varepsilon^T > \varepsilon^O$) in the direction of the spontaneous polarization. By systematically varying the lattice strains and atom positions, we also calculated the electrostrictive coefficients (Q) in the T and O structures and our data reveals that the T structure has a larger Q value relative to O. To study if increasing Sn has a tendency to facilitate the transition from O to T and provide insight into a possible mechanism, we employed Landau theory to probe the two-phase coexistence of tetragonal and orthorhombic structures at room temperature under an electric field.

We parameterized the full Landau free energy,

$$F = \alpha_1 \sum_i P_i^2 + \alpha_{11} \sum_i P_i^4 + \alpha_{12} \sum_{i>j} P_i^2 P_j^2 + \alpha_{111} \sum_i P_i^6 + \alpha_{112} \sum_{i>j}(P_i^4 P_j^2 + P_j^4 P_i^2) + \alpha_{123} \prod_i P_i^2$$

for all three compounds. The order parameter P_i ($i = 1,2,3$) is the component of spontaneous polarization along three axial directions and the Landau coefficients α_s (with α_1, α_{12} linearly dependent on temperature) are obtained from permittivity, loss tan δ, and polarization versus electric field data, together with constraints on F imposed by the phase diagram (Table S3, Supporting Information, lists all the parameters for each compound). It has been pointed out that the large piezoelectric response at the phase boundary in the BZT-xBCT system is related to the reduction of anisotropy energy with polarization[30,38,39] and elastic softening due to enhanced elastic compliance S_{33}.[38,40] The elastic compliance S_{33} of our compounds, given in Figure S5 (Supporting Information), shows that S_{33} of 3 at% Sn is not enhanced by Sn doping, suggesting that elastic softening is not associated with a large electrostrain. Following Acosta et al.,[38] we calculated the anisotropy energy G_{aniso}. **Figure 5**a shows that for the 3 at% Sn compound (red curve) the lower anisotropy energy is accompanied by a smaller energy barrier between the T and O phases compared to the 0 at% Sn compound (blue curve). The reduction of anisotropy energy and T–O energy barrier is thus the likely mechanism for the large electrostrain enhancement, making the polarization rotation easier in the 3 at% Sn compound compared to 0 at% Sn compound and leading to a larger electrostrain under an external field. We also calculated the domain structure and elastic strains in an electric field for the two compounds from phase field simulations. As shown in Figure 5b, with $E_{[01]} = 0$, both 0 at% Sn and 3 at% Sn compounds have [10] and [01] T domains and pockets of metastable O domains. The colors denote the direction of the polarization domains and the red arrows represent the polarization distributions within the domains. With $E_{[01]} = 20$ kV cm^{-1}, the [10] T domains shrink and are preferentially poled in the [01] direction. Compared to the 0 at% Sn compound, the 3 at% Sn compound has more [01] domains, indicating that polarization switching is energetically preferred in the presence of the external field in the 3 at% Sn compound. The behavior of the unipolar strain (after one cycle with remnant strain of 0.025%) along the [01] field direction is shown in Figure 5c. The larger strain obtained from the 3 at% Sn compound compared to 0 at% Sn is consistent with our experimental results (Figure 3c).

In summary, our results demonstrate that an active learning approach balancing the trade-off between exploration (using uncertainties) and exploitation (using only model predictions) provides an optimal criterion for guiding experiments in materials design. Our approach leads to the accelerated discovery of the doped compound, (Ba$_{0.84}$Ca$_{0.16}$)(Ti$_{0.90}$Zr$_{0.07}$Sn$_{0.03}$)O$_3$, for which the bipolar electrostrain at 20 kV cm^{-1} is largest in the BTO family. We attribute the optimal response at 3 at% Sn composition to the ease of switching of polarization domains in the predominantly tetragonal (T) phase at room temperature relative to the compound without Sn. Our work shows that chemical substitutions can serve as an effective route to controlling the electrostrain properties of ferroelectric oxides at the domain level.
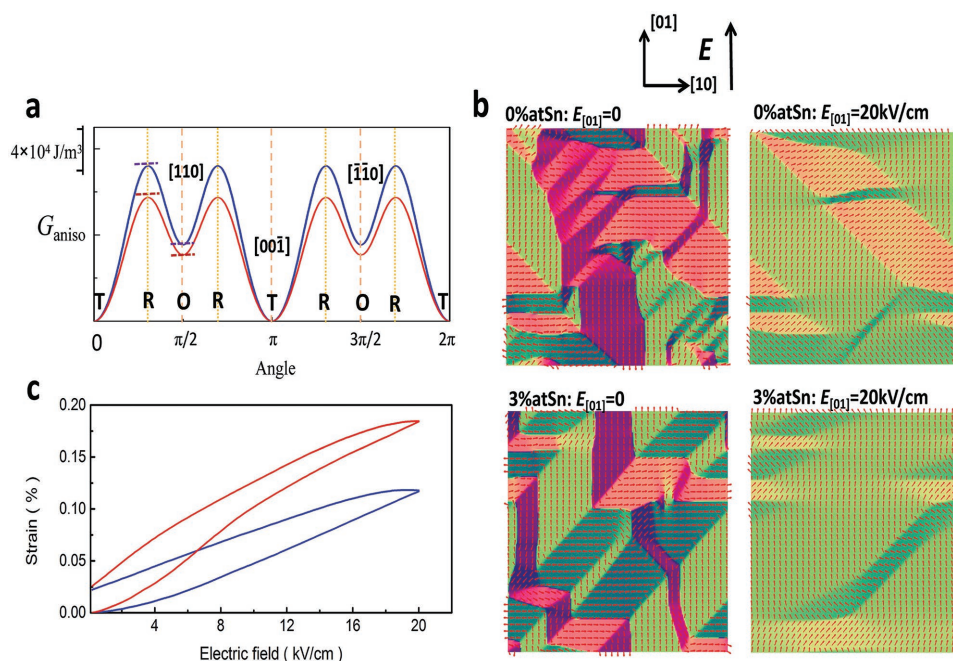
**ADVANCED
SCIENCE NEWS**

www.advancedsciencenews.com

**ADVANCED
MATERIALS**

www.advmat.de

Figure 5. a) Anisotropic energy density variation with polarization rotation in the $(1\bar{1}0)$ plane starting from the [001] direction. The 3 at% Sn compound (red curve) has lower anisotropy energy accompanied by a smaller energy barrier between T and O phases compared to the 0 at% Sn compound (blue curve). Rhombohedral (R) phase is unstable at RT. b) Domain structure of 0 at% Sn compound and 3 at% Sn compound at $E_{[01]} = 0$ and $E_{[01]} = 20$ kV cm^{-1}, respectively, illustrating the ease of rotation of the [10] tetragonal domains to the [01] direction in the case of the 3 at% Sn compound. c) Simulated electrostrain with electric field for the 0 at% Sn compound (blue curve) compared to the 3 at% Sn compound (red curve) is consistent with the experimental results for 3 at% Sn and 0 at% Sn shown in Figure 3c.

Experimental Section

$(Ba_{1.0-x-y}Ca_xSr_y)(Ti_{1.0-u-v}Zr_uSn_v)O_3$ ceramics were fabricated by a conventional solid-state method with the raw materials of $BaCO_3$ (99.8%), $CaCO_3$ (99.9%), $SrCO_3$ (99.9%), $BaZrO_3$ (99.9%), SnO_2 (99.9%), and TiO_2 (99.9%). The calcination was performed at 1350 °C for 3 h and sintering was done at 1450 °C for 3 h in air. All the samples were synthesized under the same conditions to reduce the influence of processing on the targeted property. The sintered samples for ferroelectric measurements were polished to obtain parallel sides and painted with silver electrodes. The polarization–electric field loops (P–E loops) were identified by a ferroelectric tester and electrostrains were measured by a MTI2000 photonic sensor at room temperature under a frequency of 1 Hz, all with disk-shaped samples.

Computational Section: In the Landau simulations,[41] the total free energy of the system F is written as $F = \int dV(G + f_{ela} + f_g + f_e)$, where f_{ela} is the elastic energy density, f_e is the electrostrictive energy density, and f_g is the gradient energy density, respectively. The elastic energy density can be written as $f_{ela} = \frac{1}{2}C_{ijkl}(\varepsilon_{ij} - \varepsilon_{ij}^0)(\varepsilon_{kl} - \varepsilon_{kl}^0)$, where C_{ijkl} is the elastic stiffness tensor, ε_{ij} is the total strain, and $\varepsilon_{ij}^0 = Q_{ijkl}P_kP_l$ is the spontaneous strain during the phase transformation. Q_{ijkl} is the electrostrictive coefficient. The electrostatic energy can be expressed as $f_e = -\frac{1}{2}E \cdot P - E_{ext} \cdot P$, where E_{ext} is the external applied field, and E is the electrostatic field with the electric field evaluated from the electrostatic potential φ using $E = -\nabla\varphi$. In the model the space is assumed to be charge free, therefore the equation $\nabla \cdot (-\varepsilon_0\varepsilon_b\nabla\varphi + P) = 0$ is used to solve the electric field, in which ε_0 and ε_b are permittivity of vacuum and relative background permittivity, respectively. The gradient energy density is given by $f_g = \frac{1}{2}G_{ijkl}P_{i,j}P_{k,l}$, where G_{ijkl} is the gradient coefficient. The temporal evolution of the polarization is obtained by solving the time-dependent Ginzburg–Landau equation $\frac{\delta P_i(r,t)}{\delta t} = -L\frac{\delta F}{\delta P_i(r,t)}, (i = 1,2,3)$, where r is the spatial vector and L is the kinetic coefficient. For the two compounds, the same elastic constants and electrostrictive constants were used to compare the polarization rotation behavior under an external electric field. The elastic constants of the 3 at% Sn compound are: $C_{11} = 14.0 \times 10^{10}$ N m^{-2}, $C_{12} = 11.0 \times 10^{10}$ N m^{-2}, and $C_{44} = 6.44 \times 10^{10}$ N m^{-2}, and the elastic constants of the 0 at% Sn compound are taken to be: $C_{11} = 13.5 \times 10^{10}$ N m^{-2}, $C_{12} = 11.4 \times 10^{10}$ N m^{-2}, and $C_{44} = 6.44 \times 10^{10}$ N m^{-2}. The electrostrictive constants for the two compounds are taken to be $Q_{11} = 0.08$ m^4 C^{-2}, $Q_{12} = -0.034$ m^4 C^{-2}, and $Q_{44} = 0.06$ m^4 C^{-2} with the background permittivity ε_b set at 500 (Section S6, Supporting Information, tabulates other parameters).

The DFT calculations were performed using the plane-wave pseudopotential code, Quantum ESPRESSO (QE).[42] The ultrasoft pseudopotentials with the PBEsol functional were used.[43] A plane-wave cutoff of 60 Ry was used during the ionic and electronic relaxation steps and a $4 \times 4 \times 2$ Monkhorst–Pack mesh.[44] The electric polarization was calculated using the Berry phase method,[45] as implemented in QE (see Section S6, Supporting Information, for further details).

Supporting Information

Supporting Information is available from the Wiley Online Library or from the author.

Acknowledgements

[1] Materials Genome Initiative for Global Competitiveness, https://www.whitehouse.gov/sites/default/files/microsites/ostp/materials_genome_initiativefinal (accessed: June 2017).

[2] P. Raccuglia, K. C. Elber, P. D. F. Adler, C. Falk, M. B. Wenny, A. Mollo, M. Zeller, S. A. Friedler, J. Schrier, A. J. Norquist, *Nature* **2016**, *533*, 73.

[3] T. Lookman, P. V. Balachandran, D. Xue, J. Hogden, J. Theiler, *Curr. Opin. Solid State Mater. Sci.* **2016**, *21*, 121.

[4] D. Xue, P. V. Balachandran, J. Hogden, J. Theiler, D. Xue, T. Lookman, *Nat. Commun.* **2016**, *7*, 11241.

[5] A. Mannodi-Kanakkithodi, G. M. Treich, T. D. Huan, R. Ma, M. Tefferi, Y. Cao, G. A. Sotzing, R. Ramprasad, *Adv. Mater.* **2016**, *28*, 6277.

[6] A. Jain, S. P. Ong, G. Hautier, W. Chen, W. D. Richards, S. Dacek, S. Cholia, D. Gunter, D. Skinner, G. Ceder, K. A. Persson, *APL Mater.* **2013**, *1*, 011002.

[7] S. Curtarolo, G. L. W. Hart, M. B. Nardelli, N. Mingo, S. Sanvito, O. Levy, *Nat. Mater.* **2013**, *12*, 191.

[8] J. Carrete, N. Mingo, S. Wang, S. Curtarolo, *Adv. Funct. Mater.* **2014**, *24*, 7427.

[9] V. Sharma, C. Wang, R. G. Lorenzini, R. Ma, Q. Zhu, D. W. Sinkovits, G. Pilania, A. R. Oganov, S. Kumar, G. A. Sotzing, S. A. Boggs, R. Ramprasad, *Nat. Commun.* **2014**, *5*, 4845.

[10] E. R. Dougherty, A. Zollanvari, U. M. Braga-Neto, *Curr. Genomics* **2011**, *12*, 333.

[11] D. Xue, P. V. Balachandran, R. Yuan, T. Hu, X. Qian, E. R. Dougherty, T. Lookman, *Proc. Natl. Acad. Sci. USA* **2016**, *113*, 13301.

[12] G. Hautier, C. C. Fischer, A. Jain, T. Mueller, G. Ceder, *Chem. Mater.* **2010**, *22*, 3762.

[13] K. Murphy, *Machine Learning: A Probabilistic Perspective*, Adaptive Computation and Machine Learning Series, MIT Press, Cambridge, MA **2012**.

[14] P. V. Balachandran, D. Xue, J. Theiler, J. Hogden, T. Lookman, *Sci. Rep.* **2016**, *6*, 19660.

[15] R. Dehghannasiri, D. Xue, P. V. Balachandran, M. R. Yousefi, L. A. Dalton, T. Lookman, E. R. Dougherty, *Comput. Mater. Sci.* **2017**, *129*, 311.

[16] A. I. J. Forrester, A. J. Keane, *Prog. Aerosp. Sci.* **2009**, *45*, 50.

[17] X. Liu, X. Tan, *Adv. Mater.* **2016**, *28*, 574.

[18] E. W. Sun, W. W. Cao, *Prog. Mater. Sci.* **2014**, *65*, 124.

[19] H. Zhang, C. Groh, Q. Zhang, W. Jo, K. G. Webber, J. Rödel, *Adv. Electron. Mater.* **2015**, *1*, 1500018.

[20] R. Pelrine, R. Kornbluh, Q. Pei, J. Joseph, *Science* **2000**, *287*, 836.

[21] G. H. Haertling, *J. Am. Ceram. Soc.* **1999**, *82*, 797.

[22] D. Damjanovic, *Rep. Prog. Phys.* **1998**, *61*, 1267.

[23] W. Jo, R. Dittmer, M. Acosta, J. Zang, C. Groh, E. Sapper, K. Wang, J. Rödel, *J. Electroceram.* **2012**, *29*, 71.

[24] J. Rödel, K. Webber, R. Dittmer, W. Jo, M. Kimura, D. Damjanovic, *J. Eur. Ceram. Soc.* **2015**, *35*, 1659.

[25] Y. Saito, H. Takao, T. Tani, T. Nonoyama, K. Takatori, T. Homma, T. Nagaya, M. Nakamura, *Nature* **2000**, *432*, 84.

[26] T. R. Shrout, S. J. Zhang, *J. Electroceram.* **2007**, *19*, 113.

[27] E. Cross, *Nature* **2004**, *432*, 24.

[28] K. Wang, F.-Z. Yao, W. Jo, D. Gobeljic, V. V. Shvartsman, D. C. Lupascu, J. F. Li, J. Rödel, *Adv. Funct. Mater.* **2013**, *23*, 4079.

[29] J. Wu, D. Xiao, J. Zhu, *Chem. Rev.* **2015**, *115*, 2559.

[30] W. Liu, X. Ren, *Phys. Rev. Lett.* **2009**, *103*, 257602.

[31] D. Xue, Y. Zhou, H. Bao, C. Zhou, J. Gao, X. Ren, *J. Appl. Phys.* **2011**, *109*, 054110.

[32] F. Li, L. Jin, R. Guo, *Appl. Phys. Lett.* **2014**, *105*, 232903.

[33] D. R. Jones, M. Schonlau, W. J. Welch, *J. Global Optim.* **1998**, *13*, 455.

[34] Y. Tian, X. Chao, L. Jin, L. Wei, P. Liang, Z. Yang, *Appl. Phys. Lett.* **2014**, *104*, 112901.

[35] Y. Hiruma, Y. Imai, Y. Watanabe, H. Nagata, T. Takenaka, *Appl. Phys. Lett.* **2008**, *92*, 262904.

[36] Y. Tan, J. Zhang, C. Wang, G. Viola, H. Yan, *Phys. Status Solidi A* **2015**, *212*, 433.

[37] M. Acosta, N. Novak, W. Jo, J. Rödel, *Acta Mater.* **2014**, *80*, 48.

[38] M. Acosta, N. Khakpash, T. Someya, N. Novak, W. Jo, H. Nagata, G. A. RossettiJr., J. Rödel, *Phy. Rev. B* **2015**, *91*, 104108.

[39] A. Heitmann, G. A. RossettiJr., *Philos. Mag.* **2010**, *90*, 71.

[40] L. Zhang, M. Zhang, L. Wang, C. Zhou, Z. Zhang, Y. Yao, L. Zhang, D. Xue, X. Lou, X. Ren, *Appl. Phys. Lett.* **2014**, *105*, 162908.

[41] L. Q. Chen, *Annu. Rev. Mater. Res.* **2002**, *32*, 113.

[42] P. Giannozzi, S. Baroni, N. Bonini, M. Calandra, R. Car, C. Cavazzoni, D. Ceresoli, G. L Chiarotti, M. Cococcioni, I. Dabo, A. D. Corso, S. de Gironcoli, S. Fabris, G. Fratesi, R. Gebauer, U. Gerstmann, C. Gougoussis, A. Kokalj, M. Lazzeri, L. Martin-Samos, N. Marzari, F. Mauri, R. Mazzarello, S. Paolini, A. Pasquarello, L. Paulatto, C. Sbraccia, S. Scandolo, G. Sclauzero, A. P. Seitsonen, A. Smogunov, P. Umari, R. M Wentzcovitch, *J. Phys.: Condens. Matter* **2009**, *21*, 395502.

[43] J. P. Perdew, A. Ruzsinszky, G. I. Csonka, O. A. Vydrov, G. E. Scuseria, L. A. Constantin, X. Zhou, K. Burke, *Phys. Rev. Lett.* **2008**, *100*, 136406.

[44] H. J. Monkhorst, J. D. Pack, *Phys. Rev. B* **1976**, *13*, 5188.

[45] R. D. King-Smith, D. Vanderbilt, *Phys. Rev. B* **1993**, *47*, R1651.